P-wave tomography beneath Greenland and surrounding regions-II. Lower mantle

Genti Toyokuni[1], Takaya Matsuno[1], and Dapeng Zhao[1]

[1]Tohoku University

November 21, 2022

Abstract

We study the 3-D P-wave velocity (Vp) structure of the lower mantle beneath Greenland and surrounding regions using the latest P-wave arrival-time data. The Greenland Ice Sheet Monitoring Network (GLISN), initiated in 2009, is an international project for seismic observation in these regions, and currently operating 35 seismic stations. We use a new method of global-scale seismic tomography, which sets 3-D grid nodes densely in the study region to enhance the resolution. We invert ˜5.8 million arrival times of P, pP and PP waves from 16,257 earthquakes extracted from the ISC-EHB catalog, which were recorded at 12,549 stations in the world. Our results reveal a hot plume rising from the core-mantle boundary beneath central Greenland, which is named "Greenland plume". On the other hand, the Iceland plume rises from ˜1500 km depth in the lower mantle. At depths < 1500 km, the Iceland plume might be supplied with hot mantle materials through narrow paths from a low-Vp region beneath the North Sea and/or from possible branches of the Greenland plume. We deem that, after the two plumes are joined together in the mantle transition zone (MTZ), the Greenland plume splits mainly into the Jan Mayen and Svalbard plumes in the upper mantle, supplying magmas to the Jan Mayen volcano and the geothermal area in western Svalbard, respectively. Our results also reveal a high-Vp body above the MTZ beneath northeastern Greenland. The lack of active volcanoes in Svalbard is probably due to this body obstructing the flow of the Greenland plume.

P-wave tomography beneath Greenland and surrounding regions–II. Lower mantle

Genti Toyokuni[1*], Takaya Matsuno[1], and Dapeng Zhao[1]

[1] Department of Geophysics, Graduate School of Science, Tohoku University, Sendai 980-8578, Japan

Submitted to ***Journal of Geophysical Research: Solid Earth*** in March 2020

*Corresponding author:

Genti Toyokuni

E-mail: toyokuni@tohoku.ac.jp

ORCID ID: 0000-0003-3786-207X

Key Points:

- 3-D P-wave velocity structure of the deep mantle beneath Greenland and surrounding regions is investigated.
- A hot plume rising from the core-mantle boundary beneath central Greenland is discovered and named “Greenland plume”.
- The Iceland and Greenland plumes might be interacting weakly and supplying magma to Iceland, Jan Mayen, and Svalbard.

Abstract

We study the 3-D P-wave velocity (Vp) structure of the lower mantle beneath Greenland and surrounding regions using the latest P-wave arrival-time data. The Greenland Ice Sheet Monitoring Network (GLISN), initiated in 2009, is an international project for seismic observation in these regions, and currently operating 35 seismic stations. We use a new method of global-scale seismic tomography, which sets 3-D grid nodes densely in the study region to enhance the resolution. We invert ~5.8 million arrival times of P, pP and PP waves from 16,257 earthquakes extracted from the ISC-EHB catalog, which were recorded at 12,549 stations in the world. Our results reveal a hot plume rising from the core-mantle boundary beneath central Greenland, which is named "Greenland plume". On the other hand, the Iceland plume rises from ~1500 km depth in the lower mantle. At depths < 1500 km, the Iceland plume might be supplied with hot mantle materials through narrow paths from a low-Vp region beneath the North Sea and/or from possible branches of the Greenland plume. We deem that, after the two plumes are joined together in the mantle transition zone (MTZ), the Greenland plume splits mainly into the Jan Mayen and Svalbard plumes in the upper mantle, supplying magmas to the Jan Mayen volcano and the geothermal area in western Svalbard, respectively. Our results also reveal a high-Vp body above the MTZ beneath northeastern Greenland. The lack of active volcanoes in Svalbard is probably due to this body obstructing the flow of the Greenland plume.

Plain Language Summary

Greenland and its surrounding regions have a lot of clues for understanding the global-scale tectonics and history of the Earth. Seismic tomography is a well-established method to obtain 3-D images of underground structure by inverting a huge number of seismic-wave arrival times. In this study we apply this method to the latest data recorded by a new seismograph network, and obtain detailed images of the whole mantle beneath these regions. Our high-resolution results show that what was previously considered the Iceland plume could be a complex of a true Iceland plume rising from 1500 km depth in the lower mantle and an unknown plume rising from the core-mantle boundary. We call the latter "Greenland plume". We deem that, after the two plumes are joined together in the mantle transition zone, the Greenland plume splits mainly into the Jan Mayen and Svalbard plumes in the upper mantle, supplying magmas to the Jan Mayen volcano and the geothermal area in western Svalbard, respectively. We also reveal a thick rock body with high seismic velocity in the upper mantle beneath northeastern Greenland. The lack of active volcanoes in Svalbard is probably due to this body obstructing the flow of the Greenland plume.

1 Introduction

Greenland, located in the Arctic region, is the largest island in the world. Its land area extends 2,675 km in N-S and 1,250 km in E-W [*Henriksen et al.*, 2009], spanning over 20° in the central angle of the Earth. However, at present, we can only know a small part of the island because 80% of the land area is covered by thick ice called Greenland Ice Sheet (GrIS). Geological studies of the exposure regions show that most of the crust is cratonic, which records the Earth's history of ~4 billion years since the Archean times. Therefore, the seismicity in Greenland is very low, and there is no active volcano; distribution of hot springs only shows geothermal activity in this island [*Hjartarson and Armannsson*, 2010]. On the other hand, the Mid-Atlantic Ridge is located just east of Greenland, where the North American plate on the Greenland side and the Eurasian plate on the opposite side exist and the seismicity is very active. Along the ridge, there are the Iceland and Jan Mayen volcanoes known as hot spots and a geothermal area of western Svalbard [*Dumke et al.*, 2016], showing tectonic activity and attraction of these regions (Figure 1). Especially, the Iceland hot spot is recognized as the surface expression of the Iceland plume, which has the second largest buoyancy flux estimated among all plumes on Earth, and its evolution is believed to have played a significant role in the complex continental breakup history of the northeastern Atlantic [*Barnett-Moore et al.*, 2107].

Before 2008, there were a few permanent seismic stations in Greenland, including only one station on the GrIS (station code: SUMG). Recent global climate change has been causing enhancement of cryoseismic activities mainly at the terminus of glaciers [e.g., *Ekström et al.*, 2003, 2006], which resulted in widespread attention to seismic monitoring of the GrIS. Under such circumstances, in 2009, an international project "Greenland Ice Sheet monitoring Network (GLISN)" was launched [*Clinton et al.*, 2014; *Toyokuni et al.*, 2014]. It is a project to deploy a

broadband seismic observation network in Greenland and surrounding regions, and currently the following eleven countries are collaborating: Canada, Denmark, France, Germany, Italy, Japan, Norway, Poland, South Korea, Switzerland, and the USA. The practical purposes of the GLISN project are to install and maintain new seismic and GPS stations, and to integrate the existing permanent seismic stations that had been independently operated by each country. Currently, 35 GLISN stations are in operation (see Table S1 and Figure 2 of a companion of this paper submitted at the same time to JGR; hereinafter "Paper-I"). The high-quality seismic waveforms from the GLISN network can be downloaded worldwide through the Data Management Center (DMC), a branch of the Incorporated Research Institutions for Seismology (IRIS), USA. Seismological analyses of Greenland and surrounding regions have been actively conducted using the GLISN data [e.g., *Rickers et al.*, 2013; *Mordret et al.*, 2016; *Levedev et al.*, 2017; *Levshin et al.*, 2017; *Darbyshire et al.*, 2018; *Pourpoint et al.*, 2018; *Toyokuni et al.*, 2018].

Seismic tomography is a powerful tool to obtain detailed 3-D images of underground structure. Attempt to reveal the shape and depth extent of the Iceland plume has been continued mainly by global tomography. *Bijwaard and Spakman* [2000] and *Zhao* [2001, 2004] imaged the Iceland plume as a vertical plume rising from the core-mantle boundary (CMB). *Zhao et al.* [2013] showed that, under the Iceland and Jan Mayen volcanos, a prominent localized low-velocity (low-V) zone is clearly visible from the crust down to ~500 km depth, whereas it becomes wider in the lower mantle (750–1500 km depths) and less prominent in the lowermost mantle (2300–2800 km depths). *Rickers et al.* [2013] identified two low-V conduits beneath Iceland and Jan Mayen bending in the southeastern direction at a depth of ~1000 km, connected to the same low-V zone in the lower mantle beneath the North Sea. Paper-I conducted regional tomography in this region from the surface to a depth of 700 km and revealed three low-V

conduits in the crust and upper mantle beneath Iceland, Jan Mayen, and Svalbard. The low-V conduits beneath Iceland and Jan Mayen correspond to the known Iceland and Jan Mayen plumes [e.g., *Schilling et al.*, 1999; *Rickers et al.*, 2013]. However, the low-V conduit beneath Svalbard was first discovered by them, and it was called "Svalbard plume". They also imaged a high-velocity (high-V) rock body beneath northeastern Greenland, considered as a remnant of ancient oceanic lithosphere, and mentioned the possibility that the high-V body prevents the magma flow to Svalbard and has caused the changes in the plate-spreading direction at the Mid-Atlantic Ridge when Pangea started splitting.

As outlined above, the tomographic results on the Iceland plume to date show large discrepancies. Furthermore, detailed structure in the lower mantle beneath Greenland has not been revealed. The purpose of this study is to obtain a detailed 3-D P-wave velocity (Vp) model from the mantle transition zone (MTZ) to the CMB beneath these regions by analyzing the data recorded by the latest seismic observation network (GLISN), and to improve our knowledge on the underground structures and tectonics in the study region (Figure 1).

2 Methods and Data

2.1 Global tomography

In this study we apply global tomography to reveal the whole mantle structure beneath Greenland and surrounding regions. The global tomography is a method to obtain a global 3-D seismic velocity structure by inverting a huge number of arrival-time data of earthquakes distributed all over the world [*Zhao*, 2015]. *Zhao* [2001, 2004] developed a global tomography method using the geographical grid that arranges grid nodes along latitudes and longitudes. *Zhao et al.* [2013] proposed a method of flexible grid that can be freely arranged at almost equal

intervals in the whole Earth, regardless of latitude and longitude. However, the conventional global tomography methods do not have enough resolution to examine the detailed structure beneath a specific region, because it uses the coarser grid spacing compared to the regional tomography in order to save computational resources. *Zhao et al.* [2017] adopted a multiscale grid that narrows the grid interval of the flexible grid in a target study region. As a result, despite treating the whole Earth, they could obtain detailed tomography of the study region with a resolution comparable to that of regional tomography. Theoretical arrival times are calculated through 3-D ray tracing by combining the pseudo-bending scheme [*Um and Thurber*, 1987] and Snell's law [*Zhao et al.*, 1992]. The tomographic inversion is conducted using the LSQR algorithm [*Paige and Saunders,* 1982] with damping and smoothing regularizations [*Zhao,* 2001, 2004].

2.2 Coordinate transformation

In the multi-scale tomography program by *Zhao et al.* [2017], the horizontal extent of the study region covered by a denser 3-D grid is specified in the range of latitude and longitude. In addition, since the grid is specified in a loop for latitudes and longitudes, it is difficult to arrange the grid nodes completely independent of the geographic coordinates. When we try to specify the study region located in a high-latitude region such as Greenland using ranges of latitude and longitude, an area shaped like a fan will be cut out in the horizontal direction. Therefore, in this study, we apply the coordinate transformation [*Takenaka et al.*, 2017]. It transforms all earthquakes and seismic stations from the equatorial to ecliptic coordinates so that the location (longitude, latitude) of a reference point at the center of the study region is transformed to be $(90°, 0°)$. In this study, the position of the station SUMG $(-38.461°, 72.574°)$ in the center of the GrIS is defined as the reference point as in Paper-I. As a result, the study region is moved to the

equatorial region, so when we specify the study region by ranges of latitude and longitude to make the grid interval finer, we can cut out an area shaped like a square in the horizontal direction.

2.3 Data

In order to improve the ray path coverage, we use not only the first P arrivals but also two types of later-phase data, i.e., the depth-phases (pP) and surface reflected waves (PP), from the earthquakes distributed all over the world (Fig. S1). Data are collected from the ISC-EHB catalog at the International Seismological Center (ISC) site (http://www.isc.ac.uk/) and further selected for analysis. The P, pP, and PP arrival times from 170,435 earthquakes that occurred during 1960−2016 are obtained from the ISC-EHB catalog. The coordinate transformation is applied to all the extracted latitudes and longitudes of the epicenters and the seismic stations. In order to make the hypocentral distribution uniform, the whole crust and mantle are divided into small blocks, and only one earthquake with the largest number of data in each block is extracted. For extracting as many earthquakes as possible that occurred in Greenland and surrounding regions, smaller blocks with a size of 0.1° (horizontal) × 5 km (depth) are assigned in the region within a latitude range of [−20 °, 20 °] and a longitude range of [70 °, 110 °] after the coordinate transformation (hereinafter called it “the study region”), and larger blocks with a size of 1.0° (horizontal) × 20 km (depth) are assigned in other regions. The number of earthquakes extracted finally is 16,257, and the total number of arrival time data is 5,801,577, which consist of 5,502,417 P, 174,125 pP, and 125,035 PP arrival times, recorded at 12,549 stations (Fig. 2). In addition to the GLISN stations, temporal stations in the study region (Table S1) are also used in this work.

176 **2.4 Calculation specifications**

177 We conducted two tomographic inversions as follows.

178 Case 1: The denser 3-D grid is set up from the surface to the CMB beneath the study region.

179 Case 2: The denser 3-D grid is set up from the surface to a depth of 1500 km beneath the study
180 region.

181 In both calculations, the study region is specified by the ranges of latitude [−20°, 20°] and
182 longitude [−70°, 110°] after the coordinate transformation. The flexible grid is set with a smaller
183 lateral grid interval of 55.6 km (great circle distance of 0.5° on the surface) inside the study
184 region, and with a larger lateral grid interval of 222.39 km (great circle distance of 2.0° on the
185 surface) in other regions. The grid meshes in the vertical direction in Case 1 are set at depths of
186 15, 32.5, 50, 75, 100, 140, 180, 220, 260, 300, 340, 380, 420, 460, 500, 575, 650, 725, 800, 875,
187 950, 1025, 1100, 1200, 1300, 1400, 1500, 1600, 1700, 1800, 1900, 2000, 2100, 2200, 2300, 2425,
188 2550 and 2800 km inside the study region, and 15, 50, 100, 180, 260, 340, 420, 500, 650, 800,
189 950, 1100, 1300, 1500, 1700, 1900, 2100, 2300, 2550 and 2800 km in other regions (Fig. 3).
190 The number of horizontal grid nodes at each depth is shown in Table S2.

191 The grid meshes in the vertical direction in Case 2 are set at depths of 15, 32.5, 50, 75,
192 100, 140, 180, 220, 260, 300, 340, 380, 420, 460, 500, 575, 650, 725, 800, 875, 950, 1025, 1100,
193 1200, 1300, 1400, 1500, 1700, 1900, 2100, 2300, 2550 and 2800 km inside the study region. The
194 grid meshes in other regions are the same as in Case 1. The number of horizontal grid nodes at
195 each depth is shown in Table S3.

196 The IASP91 model [*Kennett and Engdahl*, 1991] is used as the 1-D initial Vp model for
197 the tomographic inversion (Fig. S2). In all calculations, the damping parameter $\lambda_d = 15$, the

198 smoothing parameter in the vertical direction $\lambda_{sv} = 1.05 \times 10^{-2}$, and the smoothing parameter
199 in the horizontal direction $\lambda_{sh} = 9 \times 10^{-3}$ are adopted.

200 **2.5 Resolution tests and results**

201 We conducted many resolution tests including checkerboard resolution tests (CRT)
202 [*Humphreys and Clayton*, 1988; *Zhao et al.*, 2017], restoring resolution tests (RRT) [*Zhao et al.*,
203 1992, 2017], and synthetic resolution tests (SRT), to evaluate the adequacy of ray coverage and
204 spatial resolution. To conduct the CRT, we first make an input velocity model that contains
205 alternate positive and negative Vp anomalies assigned to the 3-D grid nodes; the amplitude of Vp
206 anomalies is 3% at all the nodes. The following two grid types are prepared and the inversion is
207 conducted for each grid type: (1) the lateral grid interval is 278 km (great circle distance of 2.5°
208 on the surface) inside the study region, and 556 km (great circle distance of 5° on the surface) in
209 other regions (Table S4), and (2) the lateral grid interval is 167 km (great circle distance of 1.5°
210 on the surface) inside the study region, and 334 km (great circle distance of 3° on the surface) in
211 other regions (Table S5). To conduct the RRT, we highlight the patterns of the real tomographic
212 result when constructing the RRT input Vp model, i.e., at the grid nodes with the Vp anomalies >
213 +0.6% or < −0.6% in the real tomographic model, we put constant Vp anomalies of +1.5% or
214 −1.5% for making the RRT input model. The Vp anomalies at the other grid nodes are set to zero.
215 To conduct the SRT, we construct an input model with a conduit-like −1.5% low-Vp region that
216 rises from the CMB beneath central Greenland and continues to the crust beneath Iceland. The
217 low-Vp region exists at depths ≤ 250 km, whereas Vp anomalies at greater depths are set to zero.
218 The horizontal section of the low-Vp anomaly is circular, whose central position is (longitude,
219 latitude) = (90°, 2°) on the CMB, and (98°, −6°) in the crust beneath Iceland. The radius of the
220 circle is 3°. The Vp anomalies at the other grid nodes are set to zero. Dataset for the SRT

inversion is constructed by calculating the theoretical arrival times for this input model, and random noise (-0.2 to +0.2 s) with a standard deviation of 0.1 s is added to the synthetic data to simulate picking errors of the data. Datasets for the CRT, RRT, and SRT inversions are constructed by calculating the theoretical arrival times for each input model with random noise as mentioned above. In the RRT and SRT, we use the same grid distribution in the Case 1 computation (Section 2.4).

Figures S3−S6 show the CRT results with a lateral grid interval of 278 km inside the study region. The recovery rate is defined as follows:

$$RR_i\ (\%) = \frac{(dV_P \text{ at the } i\text{th grid of the output model})}{(dV_P \text{ at the } i\text{th grid of the input model})} \times 100, \quad (1)$$

where dVp is the perturbation to Vp. On the map views (Fig. S3), the output patterns are biased to either low-Vp or high-Vp, and the resolution is clearly poor at the shallow depths (15−140 km). As for the recovery rate, the black-to-grey areas with poor recovery are dominant at depths of 15−260 km, but white areas are dominant from a depth of 300 km, and almost all areas deeper than 500 km are in white. In the cross-sections (Figs S4−S6), depth extent of the areas with good resolution can be confirmed more clearly. Similarly, Figures S7−S10 show the CRT results with a lateral grid interval of 167 km inside the study region. The areas showing good recovery are dominant at depths ≥ 300 km, as in the previous case, and can be seen in almost everywhere at depths ≥ 725 km. The two CRT results show that the resolution in our study region is ~200 km in the horizontal direction and the distances comparable to the vertical grid interval in the depth direction, from the MTZ to the CMB.

Figures S11−S14 show the RRT results. Although the Vp amplitudes of the input model tend to be smaller in the output model, and the structural ghost is more prominent in and around the MTZ, the pattern of the input model is generally recovered.

Figures S15−S18 show the SRT results. Although the low-Vp amplitude is constant in the input model at all depths, the output model shows remarkable amplitude decrease at depths ≤ 140 km. Also, as in the RRT case, the structural ghost spreads more widely in and around the MTZ (380−725 km depths). However, the pattern and amplitude of the input model are mostly recovered except around the surface, and no spurious high-Vp anomalies are generated. Spurious divisions of the plume do not appear either (e.g., C-C' section of Fig. S18). These results show that if the true plume structure has a constant low-Vp amplitude, it can be resolved well with the current dataset. In other words, disruption of the plume in the lower mantle, which appears in our tomographic results, is likely to reflect the true structure.

4 Results

In this section we describe the results obtained by our global tomography. The results of Case 1 are shown mainly, and the results of Case 2 are shown briefly.

4.1 Case 1: Setting up a denser grid in the whole mantle

The map views of the Case 1 results are shown in Figure 4. At depths of 5−80 km, only spot-like high-Vp and low-Vp zones are visible just below several stations, and in most regions, the initial Vp perturbation is not updated from zero. This is because the structure at these depths is not well resolved because the number of local earthquakes is relatively small, and so the density of seismic rays crisscrossing in the shallow regions is quite low. At depths of 120−220

km, low-Vp anomalies are remarkable beneath the Iceland and Jan Mayen volcanoes, hot springs in eastern Greenland, and the geothermal area in western Svalbard. At a depth of 120 km, they are shaped rather spotty, but at depths ≥ 160 km, they are connected together forming a band-shaped low-Vp zone. This low-Vp zone spreads further at depths of 280−490 km, and two vast low-Vp anomalies are formed beneath Iceland−Jan Mayen−eastern Greenland and Svalbard. The most remarkable high-Vp region at these depths exists off the northeastern coast of Greenland to the northeast offshore. Especially, at depths of 310−490 km, the high-Vp region extends inside the bend of the Mid-Atlantic Ridge, and seems to divide the two low-Vp regions as mentioned above. At the same depths, the high-Vp region in southwestern Greenland is also remarkable. At depth of 520−670 km, the low-Vp anomaly is prominent off the southern tip of Greenland, in addition to the low-Vp beneath Iceland−Jan Mayen−eastern Greenland. The low-Vp anomaly beneath Svalbard is also widened. These low-Vp regions seem connected together through low-Vp corridors. The regions just beneath inland Greenland are generally imaged as high-Vp anomalies.

At depths of 750−1050 km, significant low-Vp regions are confined only to those beneath Iceland. As for high-Vp regions, we can find in a wide extent beneath Ellesmere and Baffin Islands to southern Greenland, and other smaller areas beneath central Greenland and off northern Greenland to the Mid-Atlantic Ridge at depths of 750−850 km. However, at greater depths, these high-Vp regions become unclear except for that off northern Greenland. At depths of 1100−1500 km, the low-Vp region beneath Iceland moves southeast as the depth increases. There are also spot-like low-Vp anomalies beneath northern and central Greenland and Ellesmere Island (at depths ≥ 1350 km). The high-Vp anomaly is most prominent beneath southwestern Greenland at depths of 1200−1450 km.

286 At depth of 1600−1800 km, the low-Vp region beneath Iceland becomes inconspicuous,
287 and weak low-Vp areas appear in various places. Out of them, the low-Vp area beneath central to
288 eastern Greenland, and another one beneath Ellesmere Island are prominent. High-Vp anomalies
289 are hardly seen at these depths. At depths of 2000−2400 km, low-Vp anomalies located above
290 these depths connected together, forming a wide low-Vp region running NW-SE beneath
291 Greenland. Also at depths ≥ 2200 km, a clear high-Vp anomaly appears beneath the northeastern
292 coast of Greenland. At depths of 2600−2880 km, the low-Vp anomaly beneath Greenland
293 becomes more compact as getting deeper. The high-Vp anomaly beneath the northeastern coast
294 of Greenland becomes inconspicuous, but larger amplitudes of high-Vp or low-Vp regions can
295 be seen in various places, indicating that the structural heterogeneity is stronger at these depths
296 compared to the shallower depths.

297 The vertical cross-sections of the Case 1 results and the corresponding distribution of ray
298 hit count (HC) are shown in Figures 5−7 and Figures S19−S21, respectively. The 250-km depth
299 line on these figures gives a guideline to the maximum thickness of the Greenlandic lithosphere
300 [*Conrad and Lithgow-Bertelloni*, 2006]. As for the HC distribution, the areas with HC < 5, 5 ≤
301 HC < 50, and HC ≥ 50 are shown in black, gray, and white, respectively. The white color shows
302 the areas where the seismic rays pass well and the tomographic results are highly reliable. At
303 depths ≥ 300 km, almost the entire study region is in white color, which displays almost the same
304 pattern of reliability shown by the CRT.

305 As for the sections in N-S direction (Fig. 5), the A-A', B-B', and F-F' sections show
306 high-Vp anomalies tilting north or south from the surface to the mantle transition zone (MTZ).
307 However, at depths shallower than the MTZ, the regions with a better hit count are distributed
308 with the same slope as indicated in white color in Figure S19, so these high-Vp regions are likely

to have artificial shape along the seismic rays just below the stations. In the F-F', G-G', and H-H' sections through Greenland, the low-Vp anomaly that seems to be a hot plume extends from the CMB to a depth of ~1500 km. On the F-F' section beneath western Greenland, a high-Vp region that seems to be a subducted slab can be seen at depths of 1000−1500 km. In the J-J' and K-K' sections, a high-Vp region shaped like a nodule is imaged from the surface to the MTZ beneath the northeastern coast of Greenland. In the K-K', L-L', and N-N' sections in the eastern part, the hit count near the surface is improved, so the tomographic patterns shallower than the MTZ can be discussed to some extent. In these sections, clear low-Vp anomalies exist beneath the Iceland and Jan Mayen volcanoes. These low-Vp anomalies are independent beneath the two volcanoes near the surface, but are connected together in the MTZ, forming a widespread low-Vp region. In the K-K' and L-L' sections, the low-Vp anomaly beneath Svalbard is also remarkable, but the anomaly seems separated from the low-Vp region beneath Iceland and Jan Mayen due to a high-Vp body beneath northeastern Greenland.

As for the sections in E-W direction (Fig. 6), the H-H' section passing through central Greenland and Jan Mayen shows a clear plume-like low-Vp anomaly that rises from the CMB, breaks shortly at a depth of 1000 km, and reaches the Jan Mayen volcano. A low-Vp anomaly with a similar shape is also visible in the J-J' and K-K' sections beneath Iceland, but the division around 1500 km depth is remarkable, and continuity of the plume from the CMB cannot be confirmed. The K-K' section shows that the low-Vp anomaly beneath Iceland tilts eastward from the surface to a depth of 1000 km and continues almost vertically to a depth of 1500 km.

In the B-B', C-C', and DD' sections in NW-SE direction (Fig. 7), the plume-like low-Vp anomaly rising from the CMB beneath central Greenland is prominent. It extends to the northwest direction at the shallow depths, so the connection with the low-Vp anomaly beneath

Iceland located in the southeast direction is unclear. The C-C' and D-D' sections in NE-SW direction (Fig. 7), passing through central Greenland and Svalbard, clearly show a plume-like low-Vp anomaly extending from the CMB to just beneath Svalbard. It seems to be interrupted near the 410-km discontinuity due to the high-Vp body beneath northeastern Greenland.

The computation time for Case 1 was about 34 hours and 28 minutes using Xeon E5-2660 v3 (2.6 GHz, 1 core). The root-mean-square (RMS) of the total travel-time residuals is 1.60 s for the initial 1-D Vp model, but it is reduced to 1.06 s for the final 3-D Vp model.

4.2 Case 2: Setting up a denser grid at depths ≤ 1500 km

In order to investigate the effect of the grid spacing inside the study region, another calculation is performed with the denser grid distributed only from the surface to a depth of 1500 km. The resulting map views and vertical cross-sections are shown in Figures S22 and S23−S25, respectively. At depths ≤ 1500 km, there are no significant differences in the amplitudes and patterns of the tomographic results from those in Case 1, but at depths ≥ 1500 km, a mosaic-like structure due to the coarse grid distribution is dominant and thus the resulting structural patterns are strongly restricted.

5 Discussion

5.1 Consistency between regional and global tomography results

Paper-I determined a 3-D Vp model from the surface to the MTZ beneath Greenland and surrounding regions using regional tomography. In this work we determine a 3-D Vp model from the MTZ to the CMB by global tomography using a different data set and grid distribution. Since

both tomographic models have a common study region in and around the MTZ, here we discuss the consistency of the two results.

Regions with good recovery are from the surface to a depth of 700 km except around the boundary of the study region in the regional tomography and from a depth of 300 km to CMB in the global tomography. On the map views (Fig. 8 in Paper-I, and Fig. 4) for depths of 310−700 km where both results overlap, the most distinctive low-Vp anomalies beneath Iceland and Jan Mayen show clear consistency between the two results that the two low-Vp anomalies have a gap at depths of 310−370 km but merge at depths ≥ 430 km, and the amplitude of the low-Vp anomaly decreases at depths ≥ 640 km. The high-Vp anomalies beneath northeastern Greenland at depths of 310−490 km and those beneath southwestern Greenland at depths of 310−700 km also show very good agreement. The difference between the two results can only be seen in the areas where the advantages and disadvantages of both methods are strongly reflected, such as the structure near the boundary of the study region, and the amplitude of Vp anomalies. Vertical cross-sections in N-S direction through Iceland, Jan Mayen, and Svalbard also show similar patterns (Fig. 8a). The fact that the general features agree even when using different methods and datasets indicates the robustness of our tomography model.

5.2 High-Vp anomaly in the lower mantle beneath Greenland

Our results show a remarkable high-Vp anomaly at depths of 1200−1450 km beneath southwestern Greenland (Fig. 4 and the F-F' section in Fig. 5). This feature corresponds very well to a possible slab remnant suggested by *Shephard et al.* [2016] using the existing global tomography models. In this study, we have succeeded in imaging a much more detailed shape of this high-Vp anomaly by enhancing the tomographic resolution beneath Greenland.

5.3 Volcanic and geothermal activities along the Mid-Atlantic Ridge

The low-Vp anomaly beneath Iceland dips eastward to a depth of ~1000 km, then continues vertically to a depth of 1500 km, but becomes indistinct below this depth. However, there is a nearby plume-like low-Vp anomaly rising from the CMB beneath central Greenland. It looks independent of the low-Vp beneath Iceland (Fig. 8b), but it might be connected with thin low-Vp corridors that exceed the resolution of our tomography (see the J-J' and K-K' sections in Fig. 6). In order to examine the destination of the east-dipping plume, we show a vertical cross-section of our results extending to outside the study region where the denser grid is distributed (Fig. 9). We can see a low-Vp anomaly in the lower mantle beneath the North Sea, which might also be weakly connected with the plume beneath Iceland.

The low-Vp anomaly beneath Jan Mayen is weakly inclined to the west and seems connected with the plume rising from the CMB beneath central Greenland. The connection at depths 1000−1300 km seems rather unclear, but the similarity of the low-Vp slopes above and below these depths strongly suggests the continuity of the plume (Fig. 8c). Figure S26 shows a vertical cross-section expanding to outside of the region through Jan Mayen and the North Sea, but we cannot see the low-Vp continuity to the eastward. Also we cannot see any route of the low-Vp anomaly in the lower mantle beneath the Mid-Atlantic Ridge (Fig. S27).

The low-Vp anomaly beneath Svalbard is continuous with the plume beneath central Greenland (C-C' and D-D' sections in Fig. 8d). However, in the upper mantle, it seems to be interrupted by a remarkable high-Vp rock body beneath northeastern Greenland, as pointed out by Paper-I.

As described above, the low-velocity anomalies beneath the three regions might be affected by the plume rising from the CMB beneath central Greenland. This feature had sometimes been identified as the Iceland plume by previous studies, but is considered to be independent from the high-resolution images obtained in this study. Therefore we call it "Greenland plume". Figure 10 shows a schematic diagram of the mantle structure and tectonics beneath the study region revealed by this study. The Jan Mayen and Svalbard plumes in the upper mantle [Paper-I] are roughly considered as branches of the Greenland plume. We think that the Iceland plume is rather independent because the mixture of the Iceland and Greenland plumes is not complete although they seem to be merged in the MTZ. Only Iceland has many volcanoes, which probably due to the independence of the Iceland plume and the multiple sources of hot mantle material in the deeper mantle.

The images obtained in this study support the results of *Zhao et al.* [2013] showing that the Iceland plume is prominent at depths ≤ 1500 km. On the other hand, our results also have features indicating continuity of this plume from the low-Vp region beneath the North Sea as suggested by *Rickers et al.* [2013], or the vertical rise from the CMB as suggested by *Bijwaard and Spakman* [2000] and *Zhao* [2001, 2004]. We think that our results consistently integrate the various features pointed out by previous studies as the resolution has improved.

6 Conclusions

A detailed 3-D P-wave velocity model from the MTZ to the CMB beneath Greenland and surrounding regions is obtained by inverting a large number of high-quality P-wave arrival-time data recorded by the latest seismograph network. The novel tomographic model reveals the following new features.

(1) The Iceland plume rises from 1500 km depth in the lower mantle. Another plume rising from the CMB beneath central Greenland is discovered, and we call it “the Greenland plume”.

(2) At depths below 1500 km, the Iceland plume might be supplied with hot mantle materials through narrow paths from a low-velocity region beneath the North Sea on the east side and/or from possible branches of the Greenland plume.

(3) The Iceland and Greenland plumes incompletely merge together in the mantle transition zone to form a vast low-velocity region. In the upper mantle, the Greenland plume splits mainly into the Jan Mayen and Svalbard plumes, supplying hot mantle materials to feed the Jan Mayen volcano and the geothermal area in western Svalbard.

(4) A distinct high-Vp anomaly is revealed beneath southwestern Greenland at depths of 1200−1450 km, which may reflect a possible slab remnant suggested by a previous study.

Acknowledgments, author contributions, and data availability

Acknowledgments

We are grateful to Drs. Dean Childs, Kevin Nikolaus, Kent Anderson, Masaki Kanao, Yoko Tono, Seiji Tsuboi, Robin Abbott, Kathy Young, Drew Abbott, Silver Williams, Jason Hebert, Tetsuto Himeno, Susan Whitley, Orlando Leone, Akram Mostafanejad, Kirsten Arnell, and other staff at GLISN, IRIS/PASSCAL, CH2M HILL Polar Services, and Norlandair for their contributions to the field operations in Greenland. We are also grateful to ISC for providing the open-access arrival-time data archive. We thank Dr. Árni Hjartarson for providing the location data of hot springs in Greenland. We appreciate Drs. Hiroshi Takenaka, Akira Hasegawa, Satoshi Miura, Toru Matsuzawa, Ryota Hino, Tomomi Okada, and Katsutada Kaminuma for

their suggestions on an early version of this paper. This work was partially supported by research grants from Japan Society for the Promotion of Science (Nos. 15K17742, 18K03794, 24403006, 23224012, 26282105, and 26241010). The free software GMT [*Wessel et al.*, 2013] and GPlates [*Müller et al.*, 2018] are used in this study. Archiving of data from this study is underway through Zenodo. Currently these data can be seen in Supporting Information for review purposes. The arrival-time data were downloaded from the International Seismological Center (ISC) (http://www.isc.ac.uk/).

Author contributions

G.T. and D.Z. designed this study. G.T. and T.M. conducted data processing and inversion. G.T. and T.M. wrote the manuscript. All authors contributed to the interpretations and preparation of the manuscript. G.T. contributed to the installation and maintenance of six GLISN stations including three on the GrIS. The authors declare that they have no competing interests.

References

Barnett-Moore, N., Hassan, R., Flament, N., & Müller, D. (2017). The deep Earth origin of the Iceland plume and its effects on regional surface uplift and subsidence. *Solid Earth*, 8, 235–254. https://doi.org/10.5194/se-8-235-2017

Bijwaard, H., & Spakman, W. (2000). Non-linear global P-wave tomography by iterated linearized inversion. *Geophysical Journal International*, 141(1), 71–82. https://doi.org/10.1046/j.1365-246X.2000.00053.x

Clinton, J. F., Nettles, M., Walter, F., Anderson, K., Dahl-Jensen, T., Giardini, D., Govoni, A., Hanka, W., Lasocki, S., Lee, W. S., McCormack, D., Mykkeltveit, S., Stutzmann, E., &

Tsuboi, S. (2014). Seismic network in Greenland monitors Earth and ice system. *Eos, Transactions, American Geophysical Union*, 95(2), 13–24. https://doi.org/10.1002/2014EO020001

Conrad, C. P., & Lithgow-Bertelloni, C. (2006). Influence of continental roots and asthenosphere on plate-mantle coupling. *Geophysical Research Letters*, 33, L05312. https://doi.org/10.1029/2005GL025621

Darbyshire, F. A., Dahl-Jensen, T., Larsen, T. B., Voss, P. H., & Joyal, G. (2018). Crust and uppermost-mantle structure of Greenland and the Northwest Atlantic from Rayleigh wave group velocity tomography. *Geophysical Journal International*, 212(3), 1546–1569. https://doi.org/10.1093/gji/ggx479

Dumke, I., Burwicz, E. B., Berndt, C., Klaeschen, D., Feseker, T., Geissler, W. H., & Sarkar, S. (2016). Gas hydrate distribution and hydrocarbon maturation north of the Knipovich Ridge, western Svalbard margin. *Journal of Geophysical Research: Solid Earth*, 121(3), 1405–1424. https://doi.org/10.1002/2015JB012083

Ekström, G., Nettles, M., & Abers, G. A. (2003). Glacial earthquakes. *Science*, 302(5645), 622–624. http://dx.doi.org/10.1126/science.1088057

Ekström, G., Nettles, M., & Tsai, V. C. (2006). Seasonality and increasing frequency of Greenland glacial earthquakes. *Science*, 311(5768), 1756–1758. http://dx.doi.org/10.1126/science.1122112

Henriksen, N., Higgins, A. K., Kalsbeek, F., & Pulvertaft, T. C. R. (2009). *Greenland from Archaean to Quaternary, Descriptive Text to the 1995 Geological Map of Greenland,*

1:2 500 000, 126 pp. Copenhagen: Geological Survey of Denmark and Greenland. https://doi.org/10.1007/978-4-431-55360-1

Hjartarson, A., & Armannsson, H. (2010). *Geothermal research in Greenland*. Paper presented at World Geothermal Congress 2010, Bali, Indonesia.

Humphreys, E., & Clayton, R. W. (1988). Adaptation of back projection tomography to seismic travel time problems. *Journal of Geophysical Research*, 93(B2), 1073– 1085. https://doi.org/10.1029/JB093iB02p01073

Kennett, B. L. N., & Engdahl, E. R. (1991). Traveltimes for global earthquake location and phase identification. *Geophysical Journal International*, 105: 429–465. https://doi.org/10.1111/j.1365-246X.1991.tb06724.x

Lebedev, S., Schaeffer, A. J., Fullea, J., & Pease, V. (2017). Seismic tomography of the Arctic region: inferences for the thermal structure and evolution of the lithosphere. *Geological Society, London, Special Publications*, 460, 419–440. https://doi.org/10.1144/SP460.10

Levshin, A. L., Shen, W., Barmin, M. P., & Ritzwoller, M. H. (2017). Surface wave studies of the Greenland upper lithosphere using ambient seismic noise. https://pdfs.semanticscholar.org/977c/ce2101b7f9b384d38e9b051bf289a7277b54.pdf

Mordret, A., Mikesell, T. D., Harig, C., Lipovsky, B. P., & Prieto, G. A. (2016). Monitoring southwest Greenland's ice sheet melt with ambient seismic noise. *Science Advances*, 2(5), e1501538. http://dx.doi.org/10.1126/sciadv.1501538

Morgan, W. J. (1983). Hotspot tracks and the early rifting of the Atlantic. *Tectonophysics*, 94(1–4), 123–139. https://doi.org/10.1016/0040-1951(83)90013-6

503 Müller, R. D., Cannon, J., Qin, X., Watson, R. J., Gurnis, M., Williams, S., Pfaffelmoser, T.,
504 Seton, M., Russell, S. H. J., Zahirovic, S. (2018). GPlates: Building a virtual Earth
505 through deep time. *Geochemistry, Geophysics, Geosystems*, 19, 2243–2261.
506 https://doi.org/10.1029/2018GC007584

507 Paige, C. C., & Saunders, M. A. (1982). LSQR, An algorithm for sparse linear equations and
508 sparse least squares. *ACM Transactions on Mathematical Software (TOMS)*, 8(1), 43–71.
509 https://doi.org/10.1145/355984.355989

510 Pourpoint, M., Anandakrishnan, S., Ammon, C. J., & Alley, R. B. (2018). Lithospheric structure
511 of Greenland from ambient noise and earthquake surface wave tomography. *Journal of*
512 *Geophysical Research: Solid Earth*, 123, 7850–7876.
513 https://doi.org/10.1029/2018JB015490

514 Rickers, F., Fichtner, A., & Trampert, J. (2013). The Iceland–Jan Mayen plume system and its
515 impact on mantle dynamics in the North Atlantic region: Evidence from full-waveform
516 inversion. *Earth and Planetary Science Letters*, 367, 39–51.
517 https://doi.org/10.1016/j.epsl.2013.02.022

518 Schilling, J.-G., Kingsley, R., Fontignie, D., Poreda, R., & Xue, S. (1999). Dispersion of the Jan
519 Mayen and Iceland mantle plumes in the Arctic: A He-Pb-Nd-Sr isotope tracer study of
520 basalts from the Kolbeinsey, Mohns, and Knipovich Ridges. *Journal of Geophysical*
521 *Research*, 104(B5), 10,543–10,569. https://doi.org/10.1029/1999JB900057

522 Shephard, G. E., Trønnes, R. G., Spakman, W., Panet, I., & Gaina, C. (2016). Evidence for slab
523 material under Greenland and links to Cretaceous High Arctic magmatism. *Geophysical*
524 *Research Letters*, 43(8), 3717–3726. https://doi.org/10.1002/2016GL068424

Takenaka, H., Komatsu, M., Toyokuni, G., Nakamura, T., & Okamoto, T. (2017). Quasi-Cartesian finite-difference computation of seismic wave propagation for a three-dimensional sub-global model. *Earth, Planets and Space*, 69, 67. https://doi.org/10.1186/s40623-017-0651-1

Toyokuni, G., Kanao, M., Tono, Y., Himeno, T., Tsuboi, S., Childs, D., Anderson, K., & Takenaka, H. (2014). Monitoring of the Greenland ice sheet using a broadband seismometer network: the GLISN project. *Antarctic Record*, 58(1), 1–18. http://doi.org/10.15094/00009722

Toyokuni, G., Takenaka, H., Takagi, R., Kanao, M., Tsuboi, S., Tono, Y., Childs, D., & Zhao, D. (2018). Changes in Greenland ice bed conditions inferred from seismology. *Physics of the Earth and Planetary Interiors*, 277, 81–98. https://doi.org/10.1016/j.pepi.2017.10.010

Um, J., & Thurber, C. (1987). A fast algorithm for two-point seismic ray tracing. *Bulletin of the Seismological Society of America*, 77(3), 972–986.

Wessel, P., Smith, W. H. F., Scharroo, R., Luis, J., & Wobbe, F. (2013). Generic Mapping Tools: Improved Version Released. *Eos, Transactions, American Geophysical Union*, 94(45), 409. https://doi.org/10.1002/2013EO450001

Zhao, D. (2001). Seismic structure and origin of hotspots and mantle plumes. *Earth and Planetary Science Letters*, 192(3), 251–265. https://doi.org/10.1016/S0012-821X(01)00465-4

Zhao, D. (2004). Global tomographic images of mantle plumes and subducting slabs: insight into deep Earth dynamics. *Physics of the Earth and Planetary Interiors*, 146(1–2), 3–34. https://doi.org/10.1016/j.pepi.2003.07.032

Zhao, D. (2015). *Multiscale Seismic Tomography*, 304 pp. Tokyo: Springer. https://doi.org/10.1007/978-4-431-55360-1

Zhao, D., Hasegawa, A., & Horiuchi, S. (1992). Tomographic imaging of P and S wave velocity structure beneath northeastern Japan. *Journal of Geophysical Research*, 97(B13), 19909–19928. https://doi.org/10.1029/92JB00603

Zhao, D., Yamamoto, Y., & Yanada, T. (2013). Global mantle heterogeneity and its influence on teleseismic regional tomography. *Gondwana Research*, 23(2), 595–616. https://doi.org/10.1016/j.gr.2012.08.004

Zhao, D., Fujisawa, M., & Toyokuni, G. (2017). Tomography of the subducting Pacific slab and the 2015 Bonin deepest earthquake (Mw 7.9). *Scientific Reports*, 7, 44487. https://doi.org/10.1038/srep44487

Figure 1. Greenland and its surrounding regions. The color scale for altitude and legends for symbols are shown in the map. The white color denotes the Greenland ice sheet (GrIS). Red triangles: active volcanoes; red circles: hot springs; yellow triangles: GLISN seismic stations.

Figure 2. Distribution of the 16,257 earthquakes **(a)** and 12,549 seismic stations **(b)** used in the tomographic inversion. The red box indicates the target area. The thick black lines denote plate boundaries. The coordinate transformation has already been applied (see text for details).

Figure 3. Map view at a depth of 15 km **(a)** and N-S vertical cross-section **(b)** showing the 3-D grid nodes adopted for the tomographic inversion. In the target area (the red box in (a)), a denser

grid is arranged, whereas a coarser grid is set up in the surrounding crust and mantle of the Earth. The numbers atop (b) denote latitudes after the coordinate transformation.

Figure 4. Map views of Case 1 results. The layer depth is shown at the lower-right corner of each map. The blue and red colors denote high and low P-wave velocity perturbations, respectively, whose scale (in %) is shown on the right. Areas with hit counts < 5 are masked in white. The red triangles, red circles, black inverted triangles, and thin black lines denote the active volcanoes, hot springs, seismic stations, and plate boundaries, respectively.

Figure 5. Vertical cross-sections of Case 1 results along 15 profiles in the N-S direction. Location of the profiles are shown on the inset map. The 250-km depth, the 410-km discontinuity, and the 660-km discontinuity are shown in black solid lines. The thick black lines on the surface denote land areas. Other labels are the same as those in Figure 4.

Figure 6. The same as Fig. 5 but along 15 profiles in the E-W direction.

Figure 7. The same as Fig. 5 but along seven profiles in the NW-SE direction and seven profiles in the NE-SW direction.

Figure 8. Map views and vertical cross-sections showing main tectonic features in the study region and comparisons between the global tomography (this study) and the regional tomography [*Toyokuni et al.*, 2020]. **(a–d)** Vertical cross-sections along four profiles as shown in map view **(e)**. The panel (a) shows both (top) regional and (bottom) global tomographic results. The map view shows the regional tomography at 310 km depth. The symbols are the same as those in Figs. 4–8.

587 **Figure 9**. A vertical cross-section of our tomographic model along a line with irregular shape
588 passing through Canada, Greenland, Iceland, and the North Sea. This image is generated using
589 the GPlates software [*Müller et al.*, 2018].

590 **Figure 10**. Schematic diagram showing main tectonic features revealed by this study. The
591 Iceland and Greenland plumes exist in the lower mantle. The two plumes weakly merge in the
592 mantle transition zone (MTZ) and then rise as narrow plumes toward the surface. The Iceland
593 plume in the upper mantle is a continuation from the lower mantle. The Jan Mayen and Svalbard
594 plumes are considered to be mainly branches of the Greenland Plume. The high-Vp rock body
595 existing in the upper mantle beneath northeastern Greenland seems to be an obstacle to the flow
596 of the Greenland plume. The dotted arrows indicate possible connections between plumes.

597 **Figure S1**. Schematic illustration of ray paths of P, pP and PP waves. The star denotes a
598 hypocenter. The inverted triangles denote seismic stations.

599 **Figure S2**. The starting 1-D P-wave velocity model (IASP91) [*Kennett and Engdahl*, 1991]
600 adopted for 3-D tomographic inversions.

601 **Figure S3**. Map views showing the input model (left panels), output results (middle panels) and
602 the recovery rate (right panels) of the checkerboard resolution test with a lateral grid interval of
603 278 km. The depth of each layer is shown above the left panels. The open and solid circles
604 denote high and low Vp perturbations, respectively, whose scale is shown on the right. The color
605 scale of the recovery rate (in %) is also shown on the right. The red triangles, red circles, blue
606 inverted triangles, and thin black lines denote the active volcanoes, hot springs, seismic stations,
607 and plate boundaries, respectively.

608 **Figure S4**. Vertical cross-sections of the recovery rate along 15 profiles in the N-S direction
609 obtained by the checkerboard resolution test with a lateral grid interval of 278 km inside the
610 study region. Location of the profiles are shown on the inset map. The 250-km depth, the 410-
611 km discontinuity, and the 660-km discontinuity are shown in black solid lines. The thick green
612 lines on the surface denote land areas. Other labels are the same as those in Figure S3.

613 **Figure S5**. The same as Fig. S4 but along 15 profiles in the E-W direction.

614 **Figure S6**. The same as Fig. S4 but along seven profiles in the NW-SE direction and seven
615 profiles in the NE-SW direction.

616 **Figure S7**. The same as Fig. S3 but for the checkerboard resolution test with a lateral grid
617 interval of 167 km inside the study region.

618 **Figure S8**. The same as Fig. S4 but for the checkerboard resolution test with a lateral grid
619 interval of 167 km inside the study region.

620 **Figure S9**. The same as Fig. S5 but for the checkerboard resolution test with a lateral grid
621 interval of 167 km inside the study region.

622 **Figure S10**. The same as Fig. S6 but for the checkerboard resolution test with a lateral grid
623 interval of 167 km inside the study region.

624 **Figure S11**. Map views showing the input model (upper panels) and output results (lower
625 panels) of the restoring resolution test. The depth of each layer is shown above the upper panels.
626 The blue and red colors denote high and low Vp perturbations, respectively, whose scale (in %)

is shown on the right. The red triangles, red circles, blue inverted triangles, and thin black lines denote the active volcanoes, hot springs, seismic stations, and plate boundaries, respectively.

Figure S12. Vertical cross-sections of the input model (left) and output results (right) of the restoring resolution test along 15 profiles in the N-S direction. Location of the profiles are shown on the inset map. The 250-km depth, the 410-km discontinuity, and the 660-km discontinuity are shown in black solid lines. The thick black lines on the surface denote land areas. Other labels are the same as those in Figure S11.

Figure S13. The same as Fig. S12 but along 15 profiles in the E-W direction.

Figure S14. The same as Fig. S12 but seven profiles in the NW-SE direction and seven profiles in the NE-SW direction.

Figure S15. The same as Fig. S11 but for the synthetic resolution test.

Figure S16. The same as Fig. S12 but for the synthetic resolution test.

Figure S17. The same as Fig. S13 but for the synthetic resolution test.

Figure S18. The same as Fig. S14 but for the synthetic resolution test.

Figure S19. Vertical cross-sections of the ray hit count along 15 profiles in the N-S direction obtained by Case 1 computation. Location of the profiles are shown on the inset map. The 250-km depth, the 410-km discontinuity, and the 660-km discontinuity are shown in black solid lines. The thick green lines on the surface denote land areas. The red triangles denote the active volcanoes. The thin black lines in the inset map denote the plate boundaries.

Figure S20. The same as Fig. S19 but along 15 profiles in the E-W direction.

Figure S21. The same as Fig. S19 but along seven profiles in the NW-SE direction and seven profiles in the NE-SW direction.

Figure S22. The same as Fig. 4 but of Case 2 results.

Figure S23. The same as Fig. 5 but of Case 2 results.

Figure S24. The same as Fig. 6 but of Case 2 results.

Figure S25. The same as Fig. 7 but of Case 2 results.

Figure S26. The same as Fig. 9 but along a line with irregular shape passing through Canada, Greenland, Jan Mayen, and the North Sea.

Figure S27. The same as Fig. 9 but along the Mid-Atlantic Ridge.

Table S1. List of 76 seismic stations in the study region. Stations with the red background color are the GLISN stations.

Table S2. The number of lateral grids at each depth for Case 1 computation.

Table S3. The number of lateral grids at each depth for Case 2 computation.

Table S4. The number of lateral grids at each depth for the checkerboard resolution test with a lateral grid interval of 278 km inside the study region.

Table S5. The number of lateral grids at each depth for the checkerboard resolution test with a lateral grid interval of 167 km inside the study region.

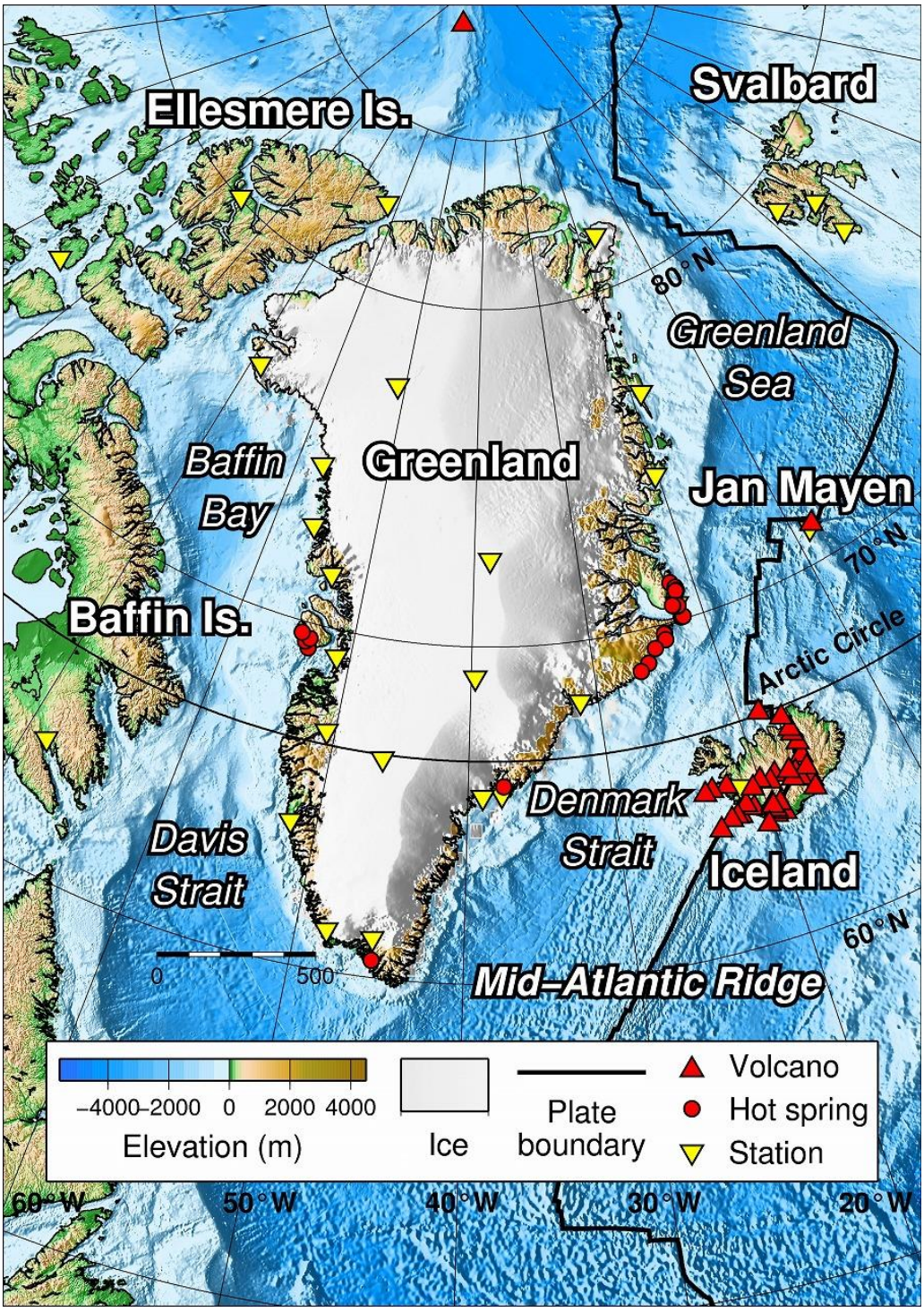

Figure 1. Greenland and its surrounding regions. The color scale for altitude and legends for symbols are shown in the map. The white color denotes the Greenland ice sheet (GrIS). Red triangles: active volcanoes; red circles: hot springs; yellow triangles: GLISN seismic stations.

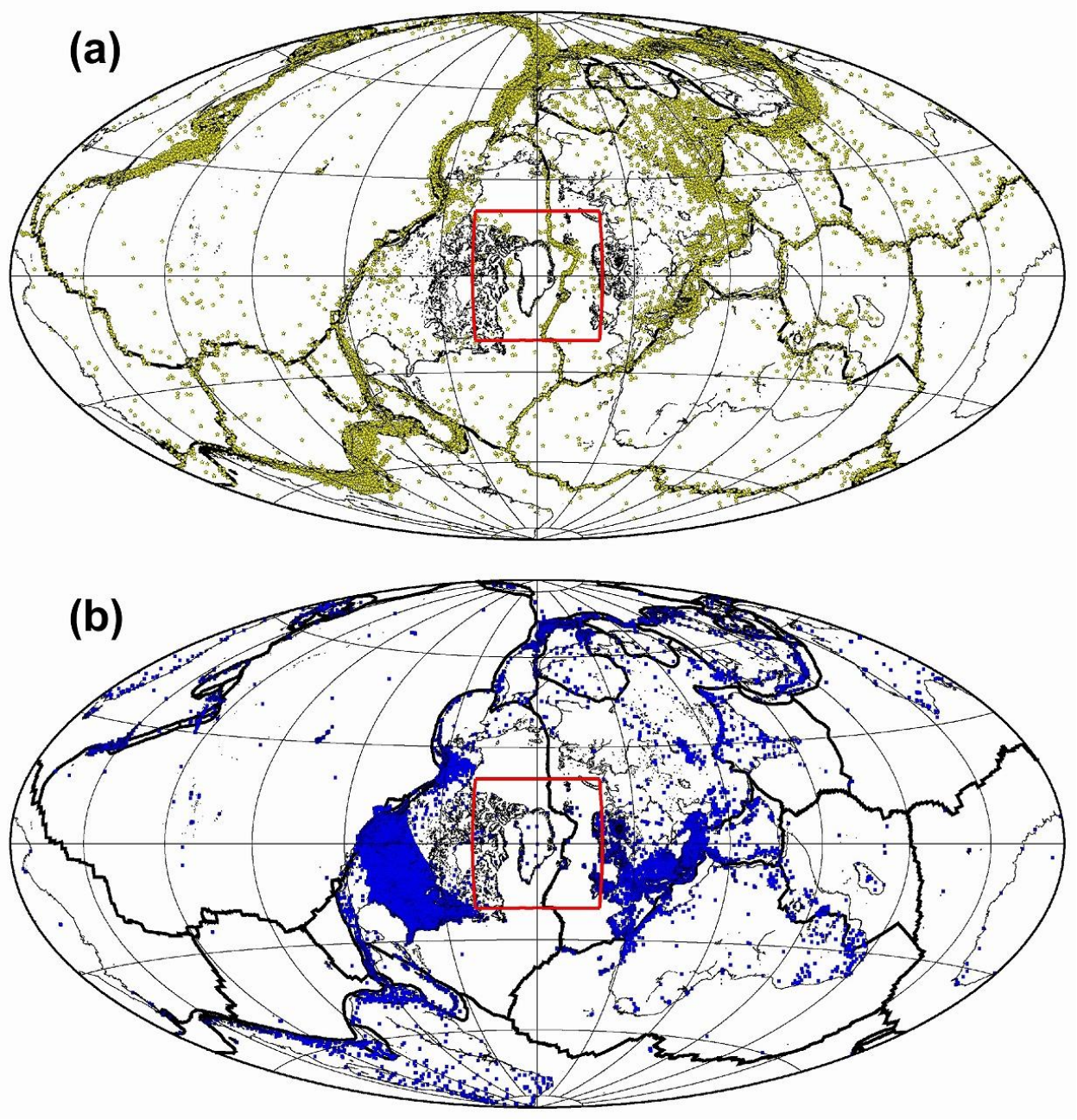

682

683

684 **Figure 2**. Distribution of the 16,257 earthquakes **(a)** and 12,549 seismic stations **(b)** used in the
685 tomographic inversion. The red box indicates the target area. The thick black lines denote plate
686 boundaries. The coordinate transformation has already been applied (see text for details).

687

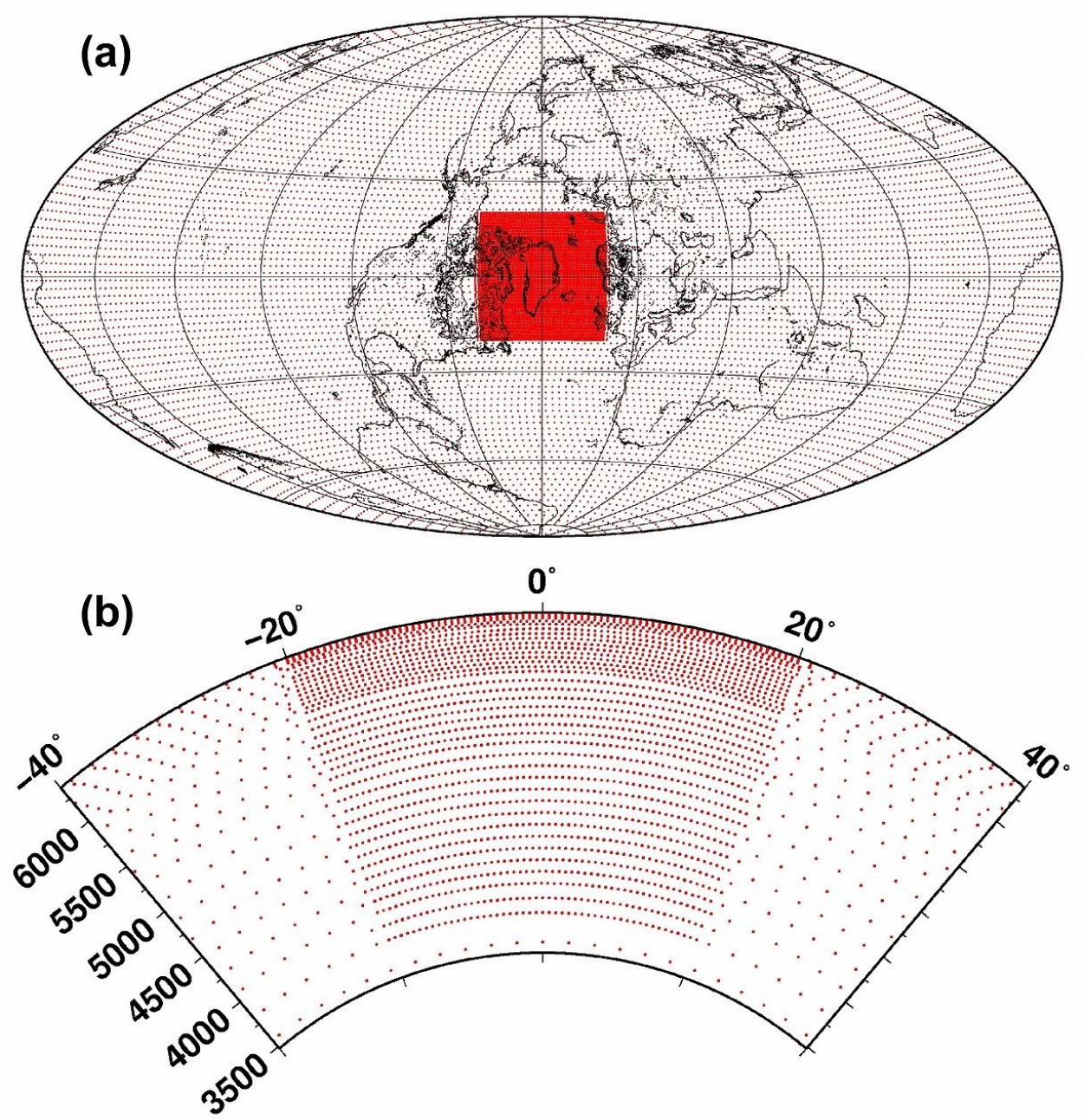

688

689 **Figure 3**. Map view at a depth of 15 km **(a)** and N-S vertical cross-section **(b)** showing the 3-D
690 grid nodes adopted for the tomographic inversion. In the target area (the red box in (a)), a denser
691 grid is arranged, whereas a coarser grid is set up in the surrounding crust and mantle of the Earth.
692 The numbers atop (b) denote latitudes after the coordinate transformation.

693

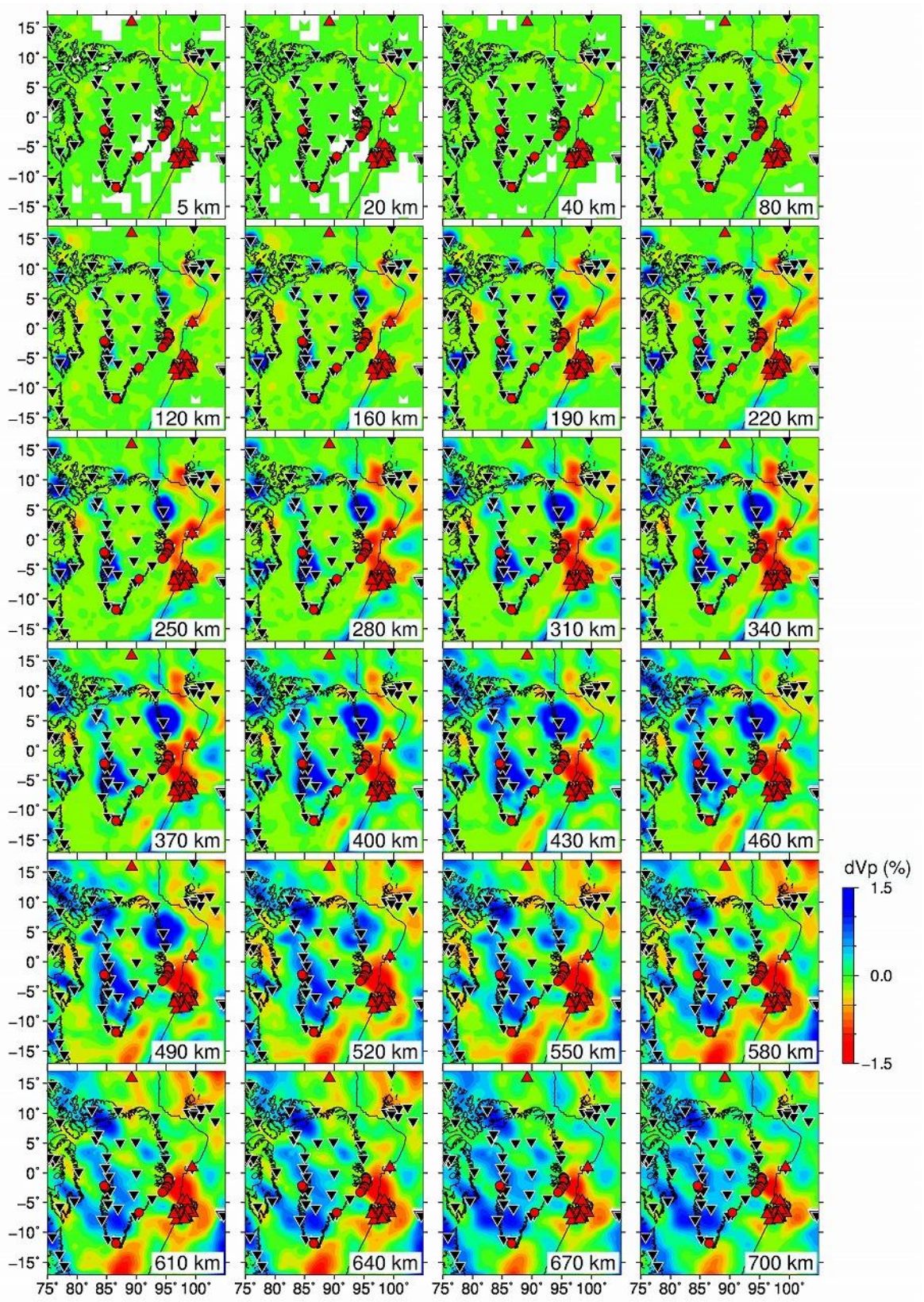

694 **Figure 4**. Map views of Case 1 results. The layer depth is shown at the lower-right corner of

each map. The blue and red colors denote high and low P-wave velocity perturbations, respectively, whose scale (in %) is shown on the right. Areas with hit counts < 5 are masked in white. The red triangles, red circles, black inverted triangles, and thin black lines denote the active volcanoes, hot springs, seismic stations, and plate boundaries, respectively.

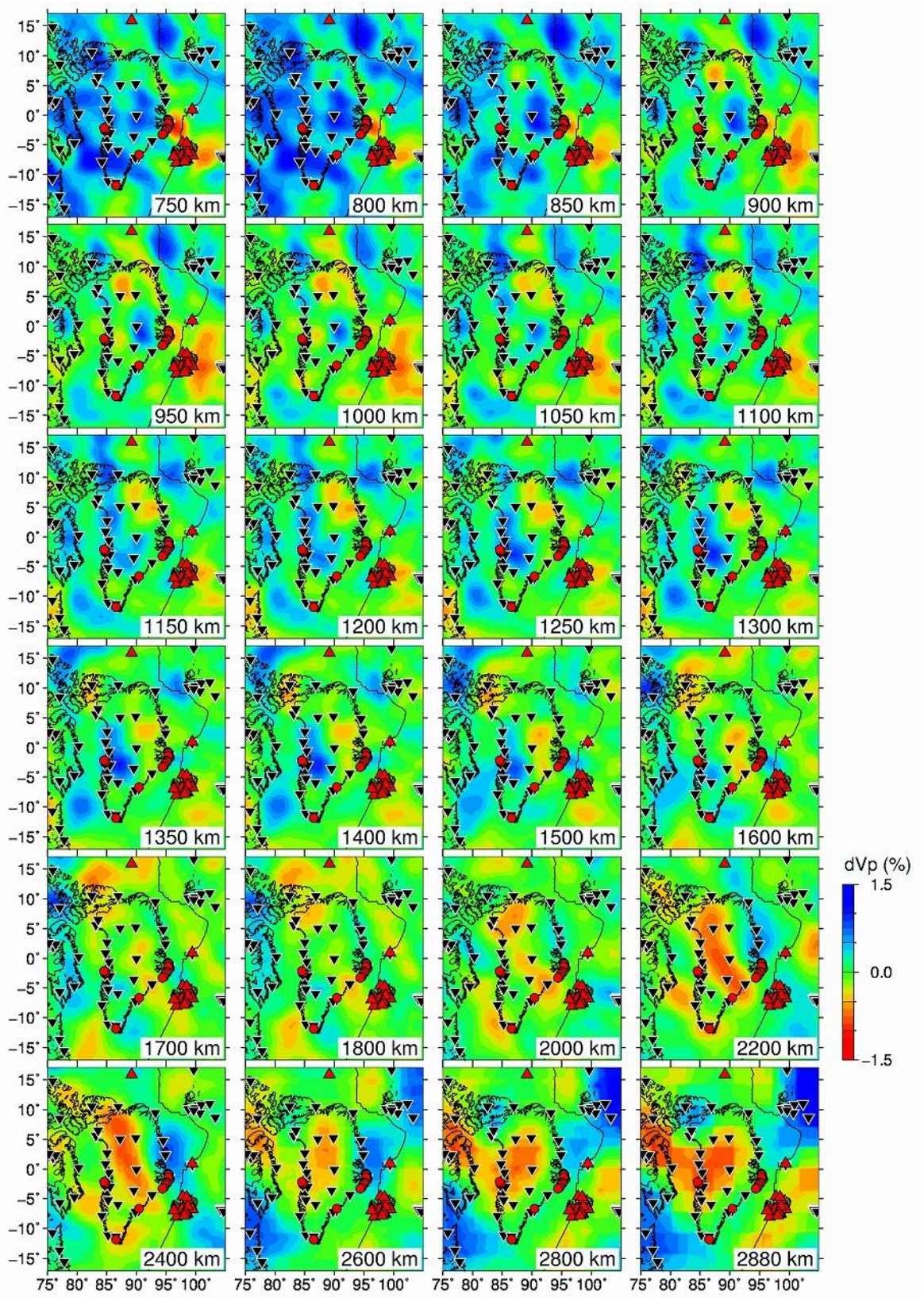

Figure 4. (continued).

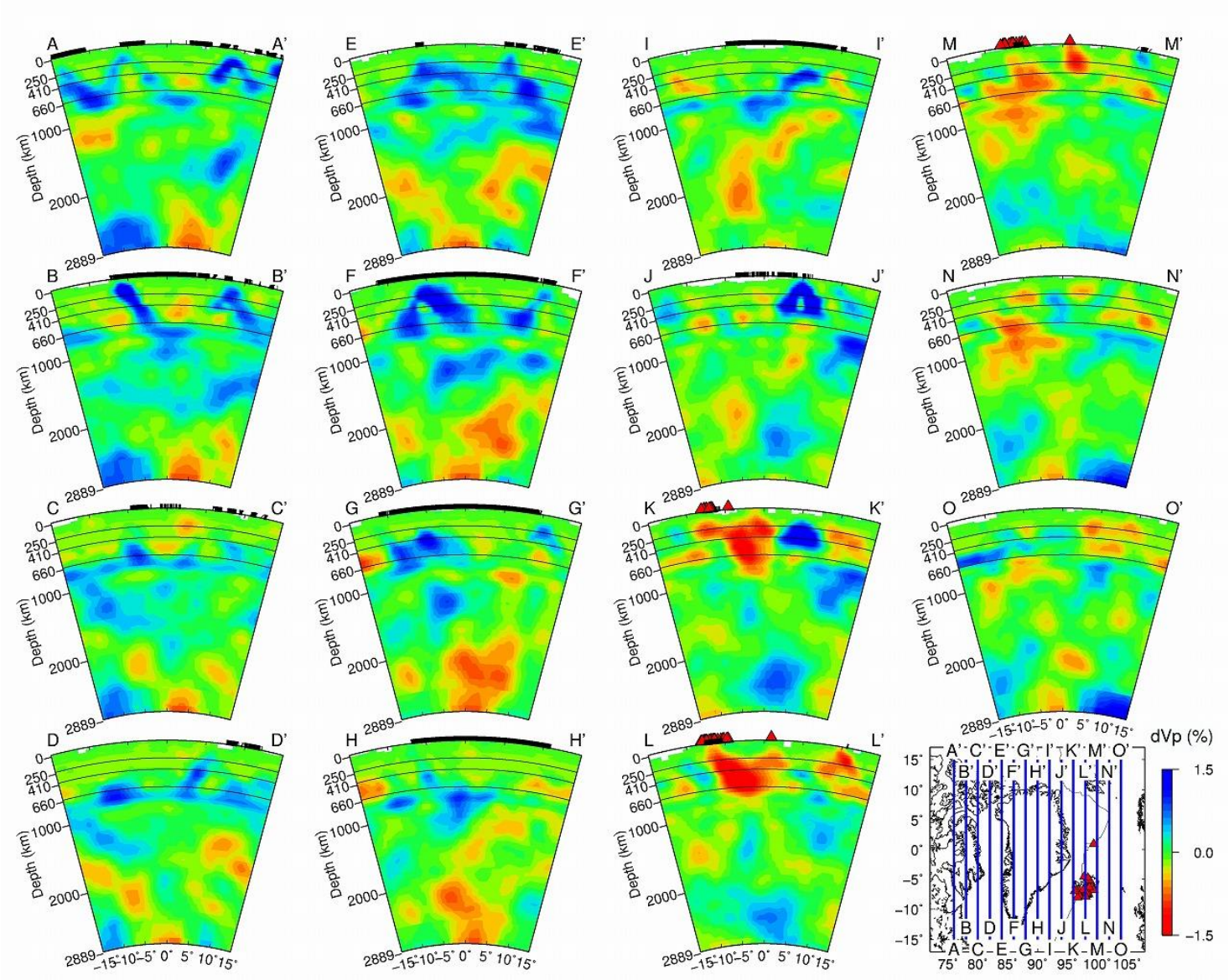

716 **Figure 5**. Vertical cross-sections of Case 1 results along 15 profiles in the N-S direction. Location of the profiles are shown on the

717 inset map. The 250-km depth, the 410-km discontinuity, and the 660-km discontinuity are shown in black solid lines. The thick black
718 lines on the surface denote land areas. Other labels are the same as those in Figure 4.
719
720
721
722
723
724
725
726
727
728
729
730

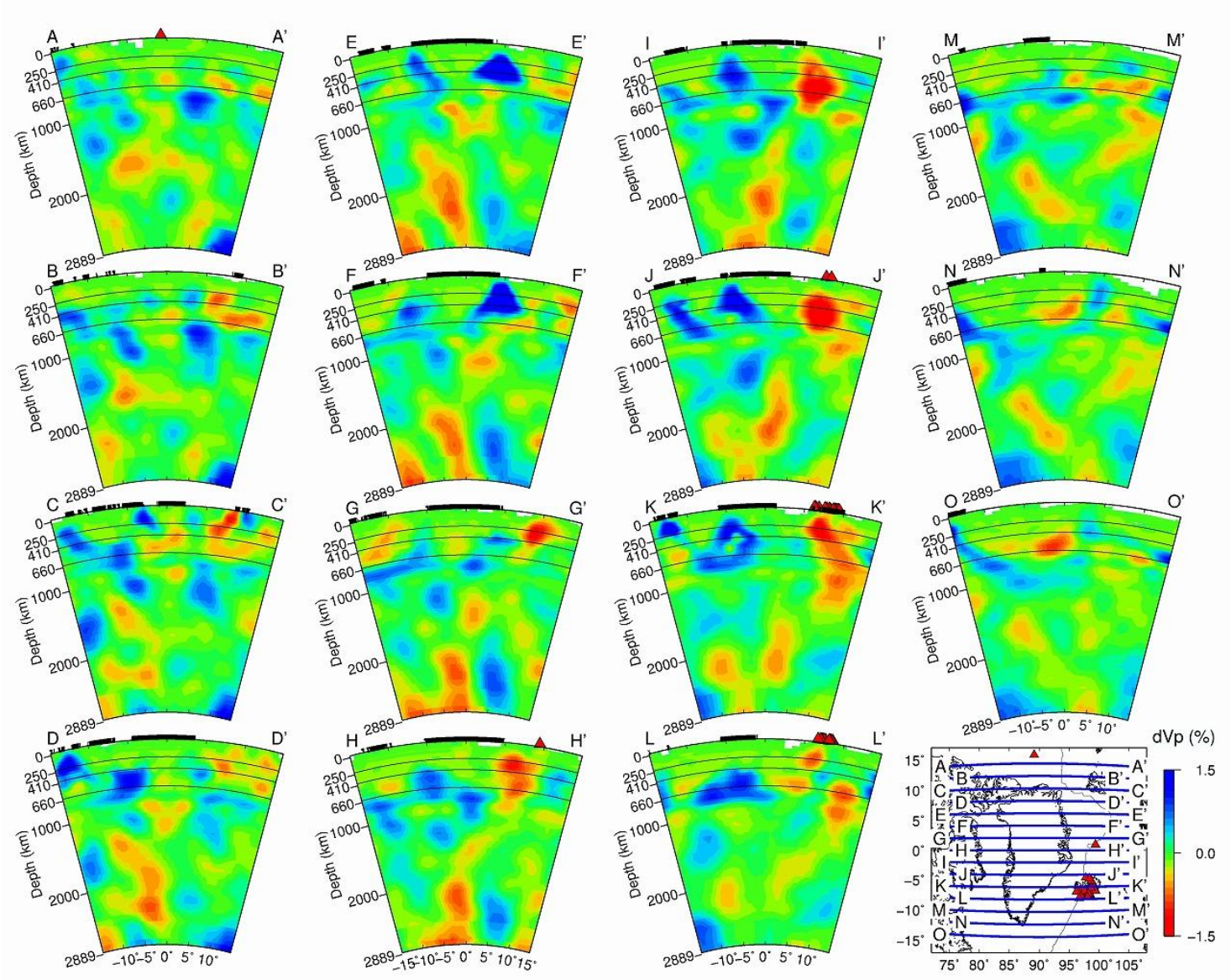

731 **Figure 6**. The same as Fig. 5 but along 15 profiles in the E-W direction.

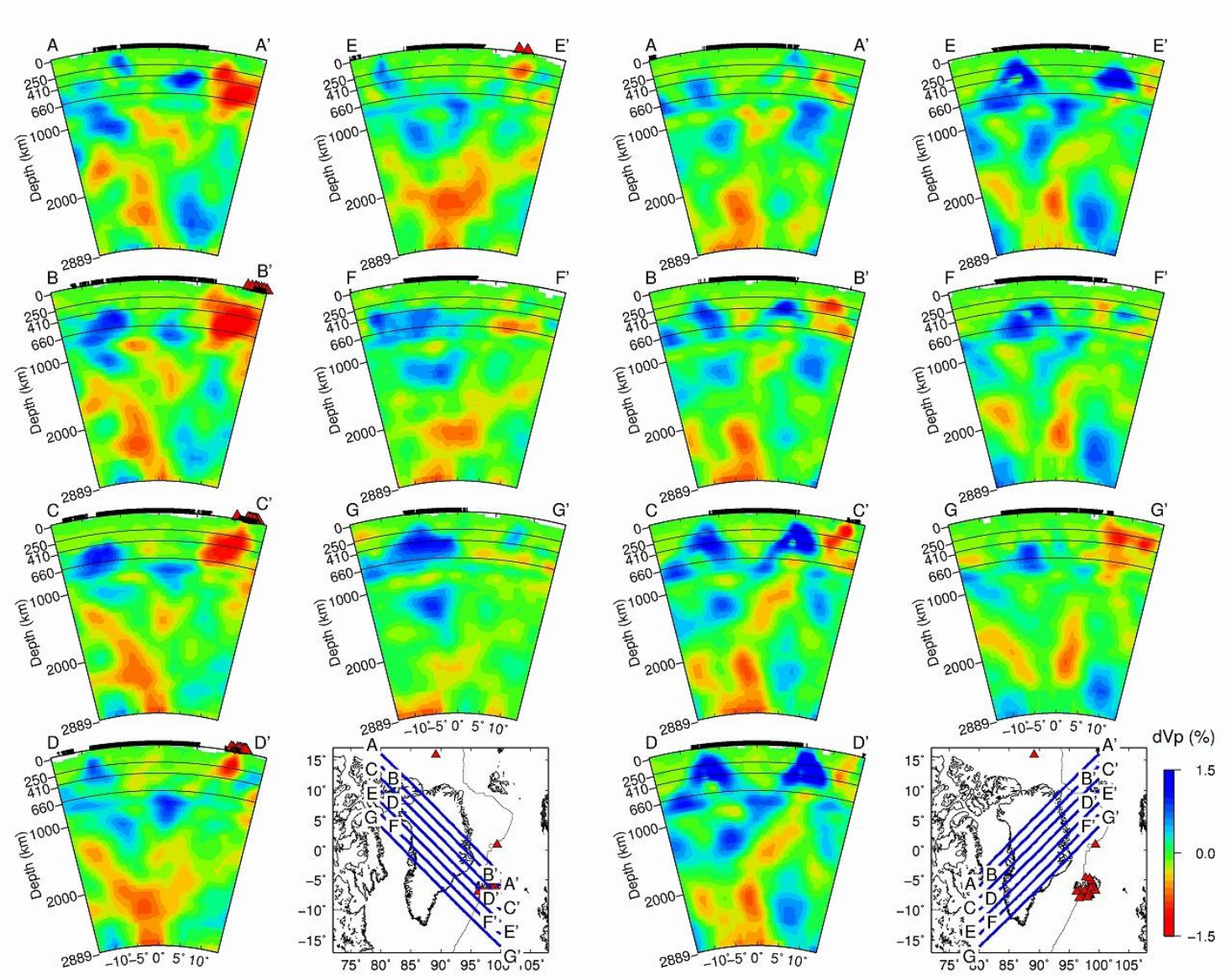

732 **Figure 7**. The same as Fig. 5 but along seven profiles in the NW-SE direction and seven profiles in the NE-SW direction.

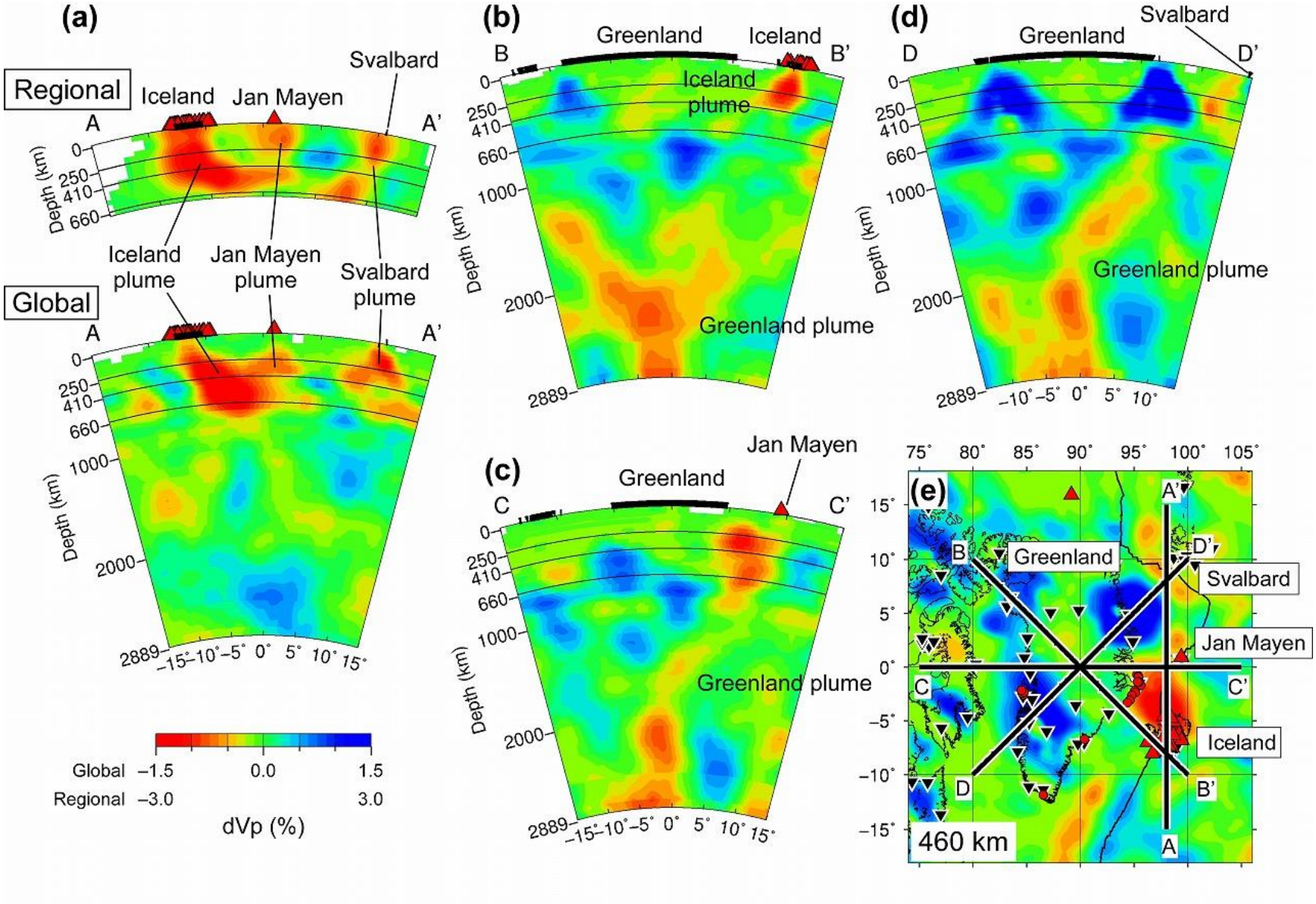

Figure 8. Map views and vertical cross-sections showing main tectonic features in the study region and comparisons between the

735 global tomography (this study) and the regional tomography [*Toyokuni et al.*, 2020]. **(a–d)** Vertical cross-sections along four profiles
736 as shown in map view **(e)**. The panel (a) shows both (top) regional and (bottom) global tomographic results. The map view shows the
737 regional tomography at 310 km depth. The symbols are the same as those in Figs. 4–7.

738

739

740

741

742

743

744

745

746

747

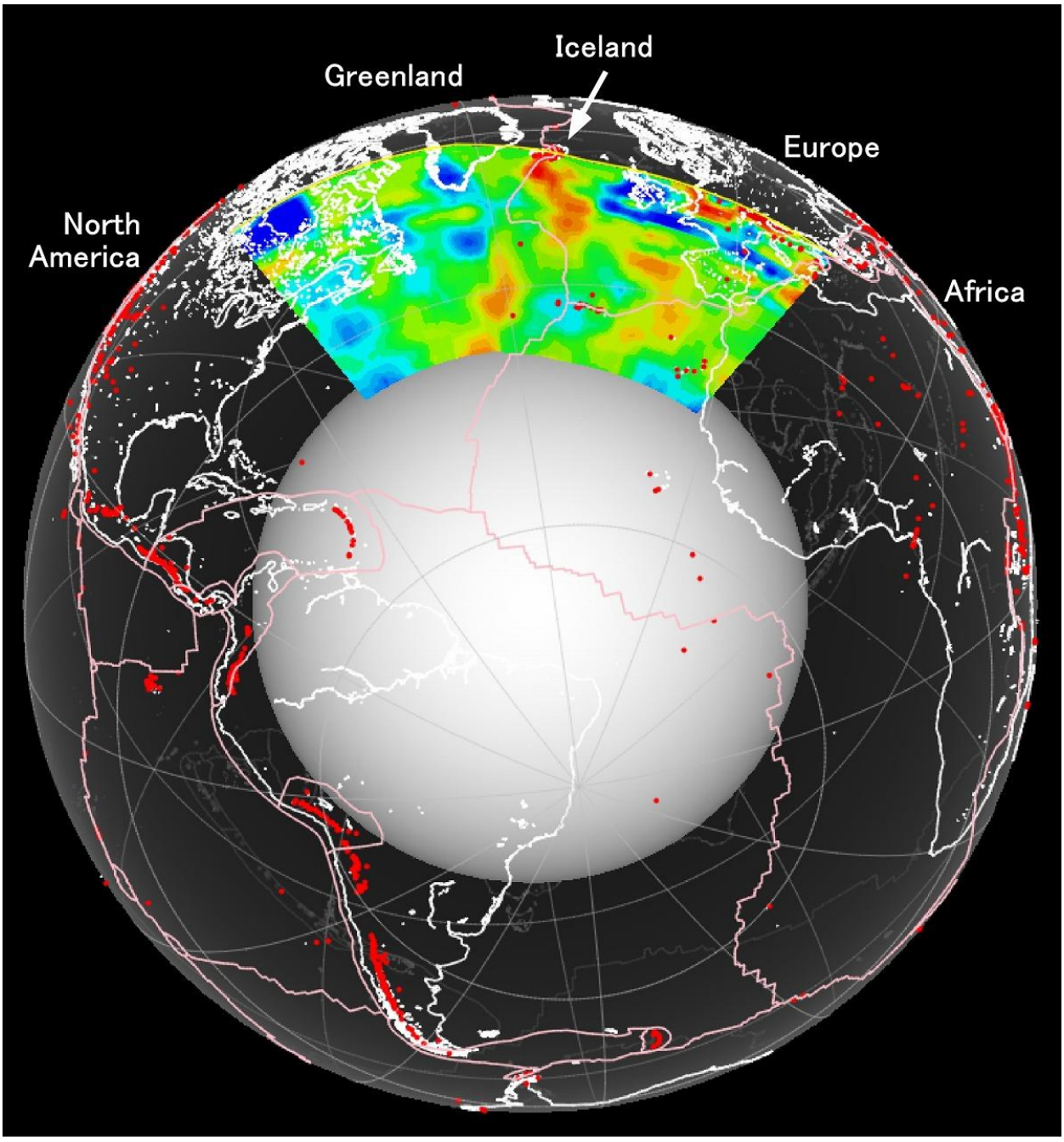

748

749 **Figure 9**. A vertical cross-section of our tomographic model along a line with irregular shape
750 passing through Canada, Greenland, Iceland, and the North Sea. This image is generated using
751 the GPlates software [*Müller et al.*, 2018].

752

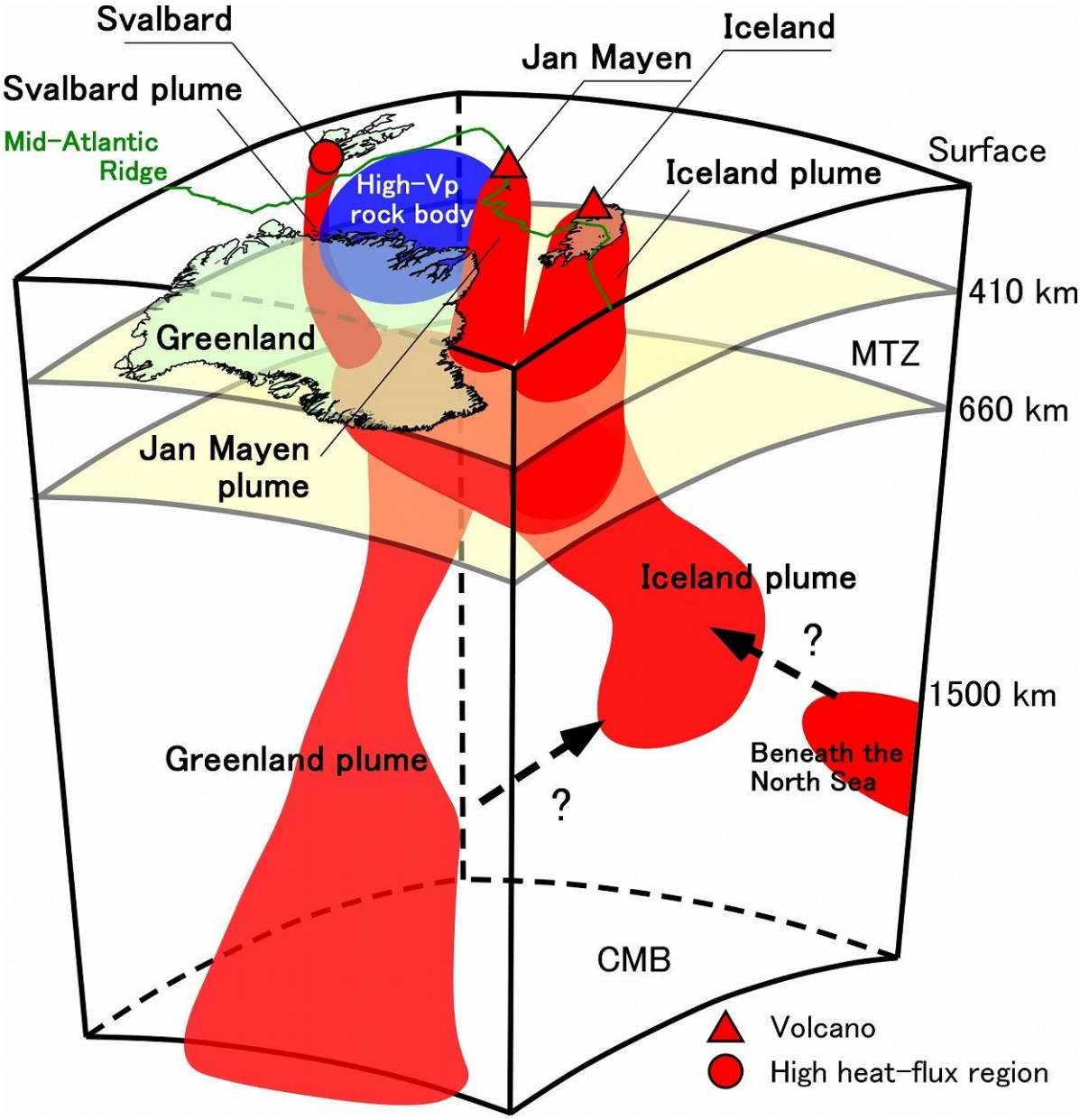

753 **Figure 10**. Schematic diagram showing main tectonic features revealed by this study. The
754 Iceland and Greenland plumes exist in the lower mantle. The two plumes weakly merge in the
755 mantle transition zone (MTZ) and then rise as narrow plumes toward the surface. The Iceland
756 plume in the upper mantle is a continuation from the lower mantle. The Jan Mayen and Svalbard
757 plumes are considered to be mainly branches of the Greenland Plume. The high-Vp rock body
758 existing in the upper mantle beneath northeastern Greenland seems to be an obstacle to the flow
759 of the Greenland plume. The dotted arrows indicate possible connections between plumes.